Research Article

Rashid Khan, Yasir A. Haleem*, Muhammad Imran Rafiq, Nadeem Abbas, Akif Zeb, Shafaq Sahar, Mohamed A. Habila, Sajid Farooq, Amna Mir, Muhammad Farooq Saleem*, and Muhammad Habib*

Synthesis of $HfSe_2$ and $CuHfSe_2$ crystalline materials using the chemical vapor transport method and their applications in supercapacitor energy storage devices

https://doi.org/10.1515/ntrev-2025-0198
received March 4, 2024; accepted June 26, 2025

Abstract: This study reports the synthesis of highly crystalline layered $HfSe_2$ and $CuHfSe_2$ using the chemical vapor transport method and the investigation of their supercapacitor behavior. Various characterizations were performed in order to confirm and ascertain the structure of the synthesized materials. The $CuHfSe_2$ electrode exhibited better supercapacitor performance due to its higher conductivity, as confirmed by experimental analysis and density functional theory calculations. The semiconducting nature of $HfSe_2$ with a 2H phase mainly impedes its electrochemical performance. Further electrochemical analyses were conducted to test the stability of both electrode materials. Moreover, these new nanocrystals can be regarded as promising supercapacitor electrode materials with good specific capacitance, excellent cycling stability, and high energy density due to the unique microstructure of such 2D materials.

Keywords: Supercapacitor, transition metaldichalcogenides, $CuHfSe_2$, single crystal, DFT

*** Corresponding author: Yasir A. Haleem,** Institute of Physics, Khwaja Fareed University of Engineering and Information Technology, Rahim Yar Khan, Punjab, 64200, Pakistan, e-mail: yasir.haleem@kfueit.edu.pk
*** Corresponding author: Muhammad Farooq Saleem,** SPIN-Lab Centre for Microscopic Research on Matter, University of Silesia in Katowice, 75 Pulku Piechoty 1A, 41-500, Chorzow, Poland; Institute of Chemistry, University of Silesia in Katowice, 9 Szkolna Str., 40-007, Katowice, Poland, e-mail: muhammad_farooq.saleem@us.edu.pl
*** Corresponding author: Muhammad Habib,** Department of Physics, COMSATS University Islamabad, Lahore campus, Lahore, Pakistan, e-mail: muhammad.habib@cuilahore.edu.pk
Rashid Khan: Zhejiang Provincial Key Laboratory of Advanced Chemical Engineering Manufacture Technology, College of Chemical and Biological Engineering, Zhejiang University, Hangzhou, 310027, China; Ningbo Titanium Core Technology (Zhejiang) Co. Ltd., Ningbo, China
Muhammad Imran Rafiq: Department of Chemical Engineering, COMSATS University Islamabad, Lahore Campus, Lahore, Pakistan
Nadeem Abbas: Research and Development Department, Nanomox Ltd., London, United Kingdom
Akif Zeb: Institute of Materials Engineering, University of Siegen, 57076, Siegen, Germany
Shafaq Sahar: College of Materials Science and Engineering, Hunan Joint International Laboratory of Advanced Materials and Technology for Clean Energy, Hunan University, Changsha, Hunan, 410082, PR China
Mohamed A. Habila: Advanced Materials Research Chair, Department of Chemistry, College of Science, King Saud University, PO Box 2455, Riyadh, 11451, Saudia Arabia
Sajid Farooq: College of Mathematical Medicine, Zhejiang Normal University, Jinhua, 321004, P.R. China
Amna Mir: Department of Physics, COMSATS University Islamabad, Lahore campus, Lahore, Pakistan

1 Introduction

With increasing concerns over the use of fossil fuels for energy generation and their environmental hazards, the scientific community is now emphasizing the utilization of alternative green energy sources and storage devices. Electrochemical capacitors, also known as supercapacitors, provide an alternative energy solution that can be used in various applications, such as renewable energy generation, electrical transportation, uninterruptible power supplies, and electrical machinery [1]. This is due to their outstanding advantages, including high specific capacitance, high power density, fast charging capability, long cycling life, large-scale production, low cost, and a wide operating voltage range [2–6].

So far, several materials have been tested as electrode materials for supercapacitor applications, including transition metal oxides, graphene, carbon nanotubes, MXene, and composites based on a combination of multiple materials [7–10]. There are also reports on metal–organic frameworks (MoFs) and even various waste material-based efficient energy storage devices [11–13]. In addition, layered transition metal dichalcogenide (TMDC) materials have emerged as an auspicious material class for electrochemical energy storage

devices [14–16]. As electrode materials, TMDCs have demonstrated promising features in various aspects, such as excellent stability when used in a single-crystal form [6], increased capacitance with phase transition [17], compatibility for on-chip integration [18], and ability to form heterostructures with other layered materials [19]. In order to further enhance the energy storage capability of layered TMDC materials, different strategies have been employed, including phase or compositional modifications [20,21], increasing active surface areas [22], and doping [23].

For example, encompassing graphene and its composites with graphene oxide and graphite oxide using the liquid-phase exfoliation technique was investigated for supercapacitor energy storage devices [24]. The authors employed a simple sonication technique for different time durations to prepare graphene, GO, and GrO composites. They found that the sample prepared with a 48-h duration showed the best results with a capacitance of 534 F/g and 94% retention due to its high conductivity and more oxygen incorporation, which led to a more dominating redox reaction phenomenon. In a recent report by Tan and coworkers [25], a reduced graphene oxide (rGO)-supported copper/manganese-based MOF composite was fabricated by adopting a low-cost technique. They tested three electrode materials, namely Cu/MnO_x-rGO, Cu/MnS_x-rGO, and Cu/MnC_x-rGO, prepared by heating at 300°C for 3 h in air, with equal-weighted sulfur under argon and at 600°C in argon, respectively. They reported a specific capacitance of >700 F/g with 92% retention. Furthermore, Gokulsaswath *et al.* [26] synthesized zirconium disulfide (ZrS_2) quantum dots using the chemical bath deposition (CBD) method and characterized them using XRD, scanning electron microscopy (SEM), and energy-dispersive spectroscopy (EDS) techniques for compositional and morphological analysis. Being a zero-dimensional material, ZrS_2 possesses a large surface area, which is an important parameter for electrochemical supercapacitors. The authors tested their energy storage properties using cyclic voltammetry, charge–discharge curves, and impedance spectroscopy in a standard three-electrode system. The synthesized ZrS_2 particles showed a specific capacitance of 101 F/g, determined using charge–discharge curves. Notably, in the aforementioned studies, the addition of carbon additives such as activated carbon and carbon black, typically comprising 10% (by mass) of the active electrode material, has become prevalent. To a certain extent, this practice obscures the true intrinsic behaviour of the materials under investigation. The addition of carbon-based additives increases conductivity, reduces voltage drop, and ultimately enhances performance significantly compared to the original value.

Among several layered TMDC materials, although hafnium diselenide ($HfSe_2$) has been explored for several applications, it has still not been considered for energy storage applications [27,28]. In this work, we have synthesized hafnium diselenide single crystals using the chemical vapor transport (CVT) method. The grown crystals were employed as an electrochemical supercapacitor electrode material, and clear insights into their intrinsic behavior were reported without using any carbon additives. $HfSe_2$ single crystals were further doped with copper, and comparative analysis was performed between Cu-doped ($CuHfSe_2$) and -undoped $HfSe_2$. The grown single crystals exhibited enhanced and stable performance with $CuHfSe_2$ under a three-electrode measurement setup. The Cu-doped electrode expedited electronic conductivity, which in turn improved the specific capacitance and stability, demonstrating potential for this newly tested 2D TMDC material in energy storage devices.

2 Experimental

2.1 Materials synthesis and electrode preparation

The reagents utilized in this study were purchased from Sinopharm Chemical Reagent and Sigma-Aldrich and were utilized without further purification steps. For CVT growth, stoichiometric amounts of hafnium–selenide and copper–hafnium–selenide powders were mixed with 20 mg iodine as a transport agent. In the next step, powder materials were put into the quartz ampoules with an inner diameter and length of 5 mm and 25 cm, respectively. After this, ampoules were evacuated to a vacuum of 10^{-3} Torr and tightly sealed. Finally, the sealed tubes were placed in a double temperature zone split-type furnace and heated at 850 and 950°C for a duration of 5 days. After 5 days, the furnace was cooled to room temperature, and the ampoule tubes containing $HfSe_2$ and $CuHfSe_2$ crystals (ranging in size from several microns to millimeters) were obtained. It is worth mentioning that erstwhile quartz ampoules were thoroughly cleaned with diluted HNO_3 and in succession washed with DI water and dried in an oven at 60°C. For the electrode preparation, bulk millimeter-sized single crystals of $HfSe_2$ and $CuHfSe_2$ were cleaned with IPA and then thoroughly ground to obtain a very fine powder. Then, 2 mg of this powder was added to a DI water, IPA, and Nafion combined solution in volumes of 750, 250, and 10 µl, respectively, and sonicated for several hours. Then, 5 µl of the prepared solution was placed on a working electrode (3 mm diameter) and used for measurements after drying in an oven at room temperature (Figure 1).

SEM images were taken using a ZEISS Gemini Field Emission SEM, and the same was used to obtain elemental EDS spectra of the samples. X-ray photoelectron spectroscopy (XPS) was performed using an ESCALAB 250Xi X-ray photoelectron spectrometer. The crystal structure of the grown materials was analyzed with X'Pert Pro Super (Philips Co., Netherlands). For the SEM, EDS, and XPS measurements, fine powder-like samples were prepared by grinding the flakes, while for XRD characterization, one large-sized flake was selected and used after proper washing. All electrochemical measurements were conducted on a nickel foam utilizing finely ground powder of our sample materials. These measurements were performed using a Corrtest Instrument Potentiostat.

2.2 Calculation methods

First-principles calculations were performed using the CASTEP module with the Generalized Gradient Approximation. The exchange-correlation functional of Perdew, Burke, and Ernzerhof was chosen. Norm-conserving pseudopotentials with Koelling–Harmon relativistic treatment used for calculations thus improved the electronic properties, such as lattice constant, band, and partial density of states (PDOS). In this work, norm-conserving pseudopotential of 440 eV and a set of 10 × 10 × 4 k-point scheme were used for the relaxation of $HfSe_2$ and Cu-doped $HfSe_2$, whereas all structures were fully relaxed with a force tolerance of 0.01 eV/A.

3 Results and discussion

X-ray diffraction patterns of $HfSe_2$ and $CuHfSe_2$ single crystals showed major peaks along the (001), (003), (004), and (005) planes, as shown in Figure 2(a). The XRD patterns obtained showed a prominent crystalline nature of the grown $HfSe_2$ single crystals, which retained the 2-H phase and matched well with the standard JCPDS card no. 37-1488.

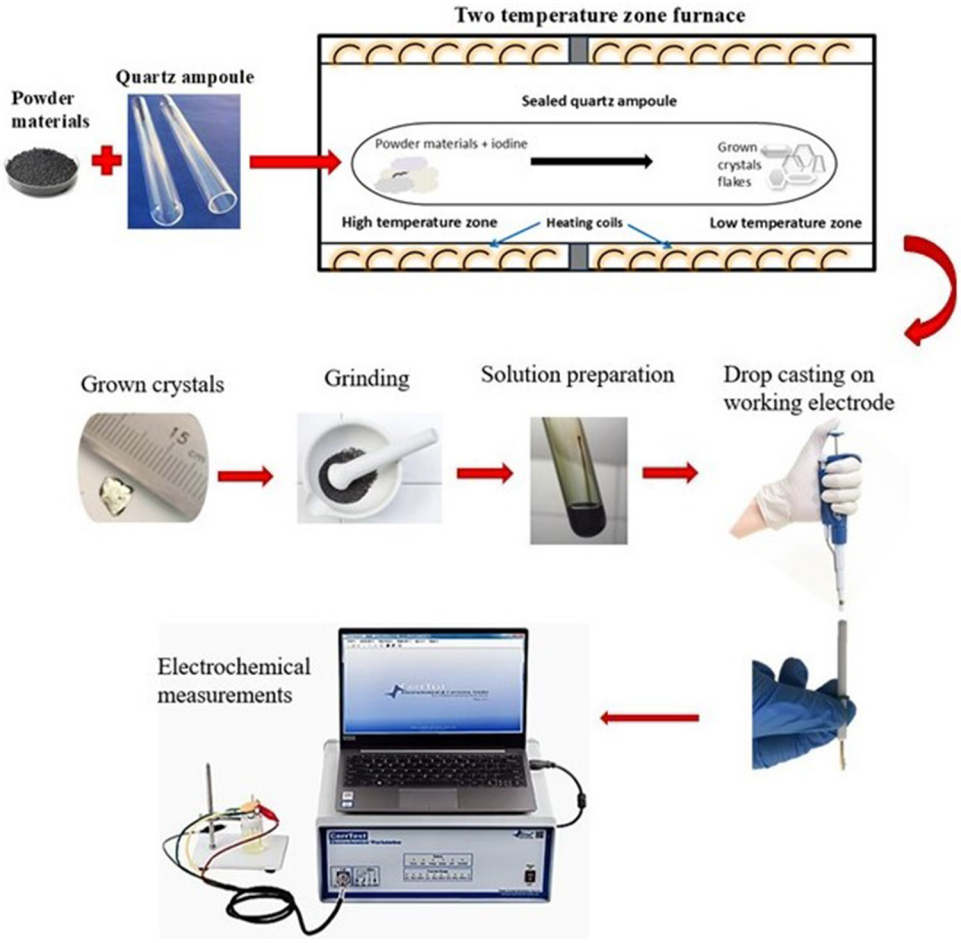

Figure 1: Schematic illustration of CVT growth setup using a double-zone furnace and the electrode preparation process.

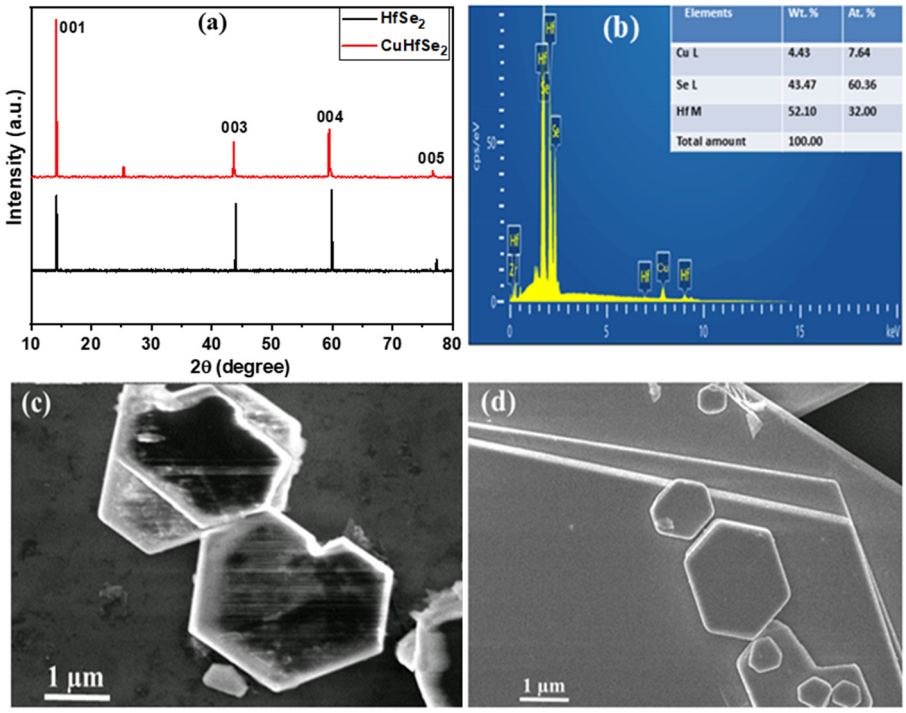

Figure 2: (a) XRD patterns of $HfSe_2$ and $CuHfSe_2$ single crystals, (b) EDS of $CuHfSe_2$, and (c) and (d) SEM images of $HfSe_2$ and $CuHfSe_2$ single crystals.

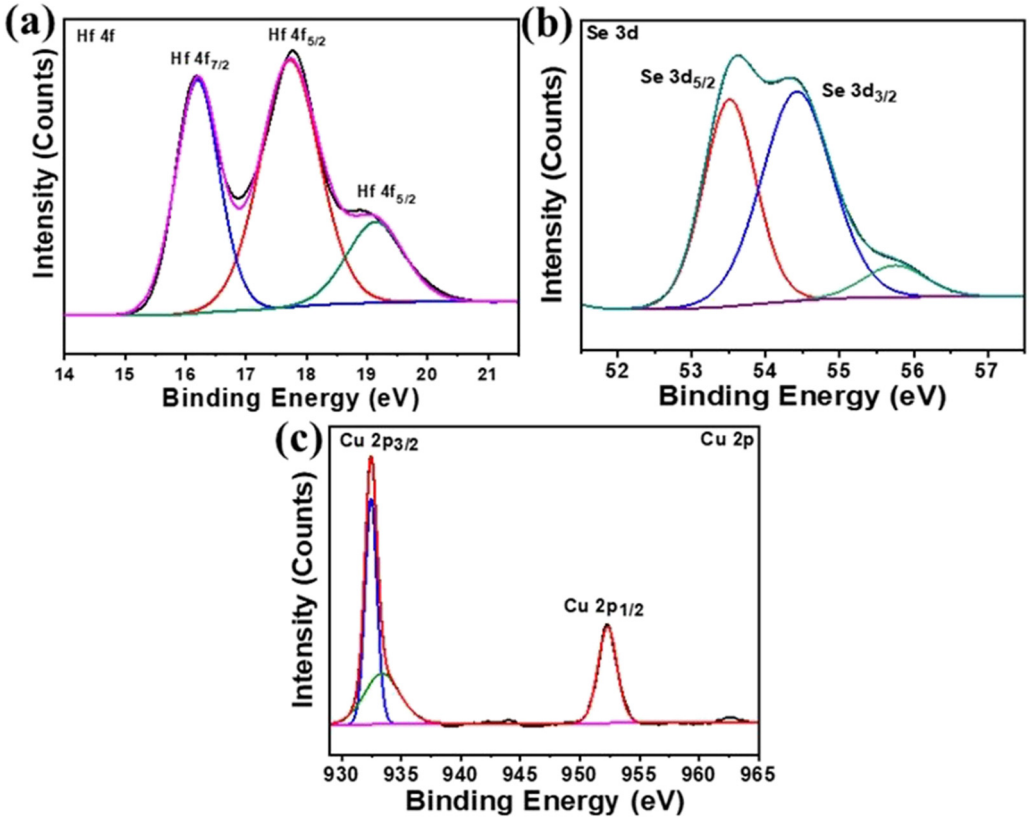

Figure 3: XPS spectra for the (a) Hf 4f, (b) Se 3d, and (c) Cu 2p core levels.

XRD spectra of $CuHfSe_2$ further revealed that the peak positions shifted to lower degrees compared to $HfSe_2$, which confirmed successful doping of Cu atoms into $HfSe_2$. These results are in accordance with the previously reported works of TMDC doping with transition metals [29,30]. The slight shift in peaks occurred due to a mismatch in the ionic crystal radii of copper and hafnium (Cu^{+1} ~ 91 pm, Hf^{+4} ~ 85 pm) [31]. A new peak at around 25° also appeared in the Cu-doped $HfSe_2$ XRD spectrum. The appearance of this peak may be attributed to a minor presence of Cu_2Se in the sample; however, it did not alter or disrupt the original structure of the grown material, as evidenced by the presence of other sharp and intense diffraction peaks corresponding to $CuHfSe_2$.

The EDS was performed to study the elemental peak analysis of the $CuHfSe_2$ material, as presented in Figure 2(b). The presence of Cu peaks clearly manifests the existence of an adequate proportion of Cu in the synthesized material.

Scanning electron microscopy images of the $HfSe_2$ and $CuHfSe_2$ crystals are shown in Figure 2(c) and (d), respectively. The figures revealed that most of the grown crystals are in hexagonal shape, with sizes in several microns.

Figure 3 shows the chemical composition of $CuHfSe_2$ single crystals performed using XPS. Figure 3(a) depicts the Hf 4f spectra with two main binding energy peaks of $4f_{7/2}$ and $4f_{5/2}$ appearing around 16.1 and 18.2 eV, respectively. These two peaks correspond to $HfSe_2$, while a small peak observed at 19.2 eV confirmed the presence of HfO_x. Se 3d scan, shown in Figure 3(b), is composed of two foremost peaks, which are Se $3d_{3/2}$ (~54.47 eV) and Se $3d_{5/2}$ (~53.58 eV), attributed to Hf–Se bonding along with a small peak of the Se–Se bonding state in the grown sample (~55.8 eV). Figure 3(c) illustrates the Cu 2p spectra with binding energy peaks for Cu $2p_{3/2}$ and Cu $2p_{1/2}$ appearing at around 932.5 and 952.4 eV, respectively. The occurrence of these characteristic peaks matches well with the

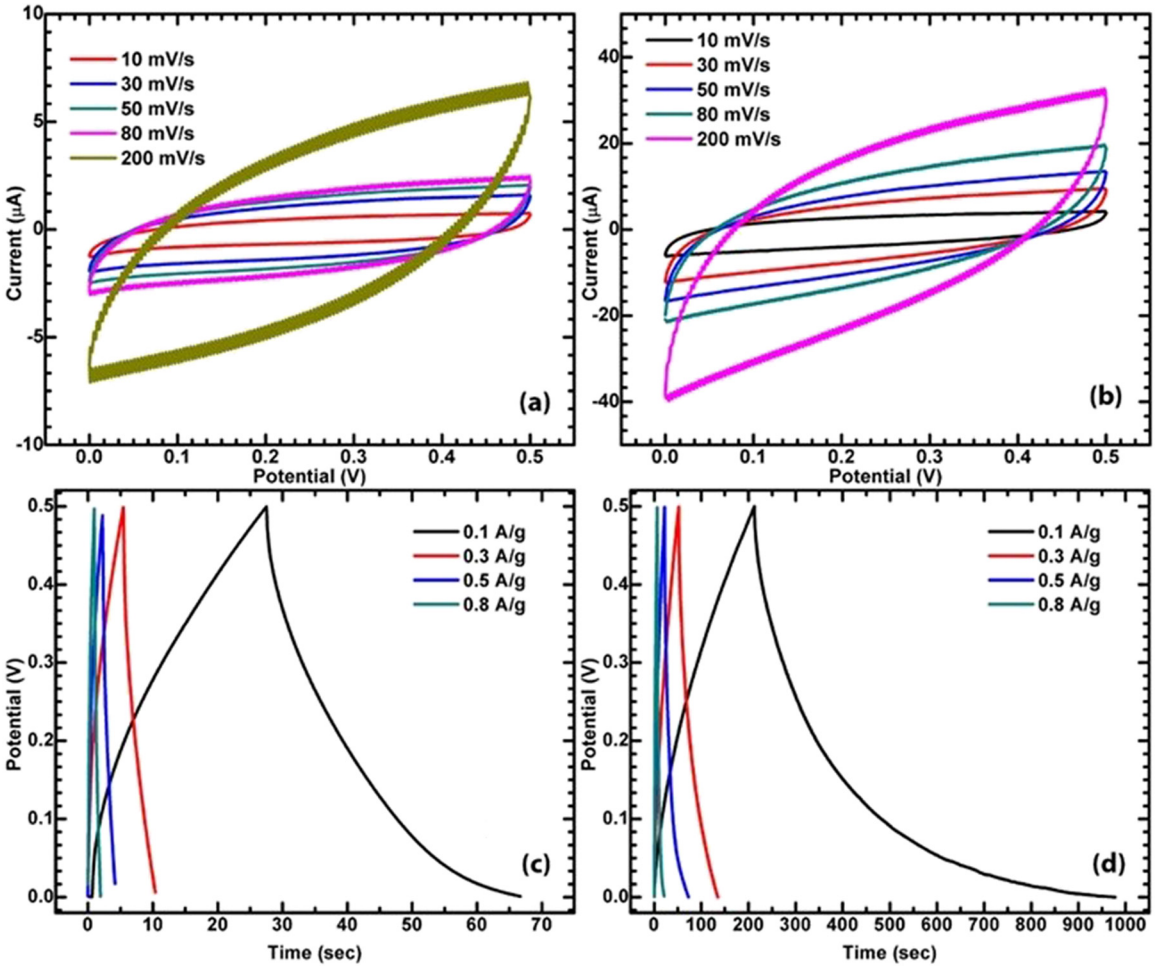

Figure 4: Cyclic voltammograms of (a) $HfSe_2$ and (b) $CuHfSe_2$. Charge–discharge profiles of (c) $HfSe_2$ and (d) $CuHfSe_2$ electrodes.

previously reported work [28,32]. $HfSe_2$ is known to be more prone to oxidation compared to its other counterpart TMDCs [33]. The manifestation of the HfO_x phase in the XPS spectra may be due to the exposure of samples to air during characterization, but not during the growth (since the sample tubes were vacuumed and sealed for crystal growth).

To unveil the electrochemical performance of the prepared electrode materials, cyclic voltammetry (CV) was performed in the potential range from 0 to 0.5 V with scan rates ranging from 10 to 200 mV s^{-1}, as shown in Figure 4(a) and (b). The galvanostatic charge–discharge profiles of $HfSe_2$ and $CuHfSe_2$ are shown in Figure 4(c) and (d), respectively. The capacitance values of the prepared electrodes were calculated using CV profiles. First, the area under the CV curve was calculated by integrating the curve, whereas equation (1) was used to determine the capacitance values [8]:

$$C_{sp} = 2[mv(V_a - V_b)]^{-1}\int I(V)\mathrm{d}v, \quad (1)$$

where m is the mass of the electrodes, v is the scan rate, $V_a - V_b$ is the potential window, and $\int I(V)\,\mathrm{d}V$ is the integrating CV area. The highest calculated capacitance values were 44.7 and 151.83 F/g for $HfSe_2$ and $CuHfSe_2$ electrodes, respectively, at a scan rate of 10 mV s^{-1}. It can be observed that all CV curves show a semi-rectangular shape at all scanning rates, exemplifying the presence of electrochemical double-layer capacitor (EDLC) behavior. $CuHfSe_2$ electrodes exhibited significantly higher capacitance than undoped $HfSe_2$, primarily due to improved electrical conductivity. It is well known that conductivity, surface area, porosity, functional group attachment, and interlayer spacing are the main contributing factors for efficiency enhancement. The electrode materials prepared were tested for stability with 5,000 charge–discharge cycles. Figure 5(a) depicts the stability trend of the $CuHfSe_2$ electrode with more capacitance retention compared to the $HfSe_2$ electrode, as shown in Figure 5(b). The initial capacitance loss observed during the early charge–discharge cycles can be attributed to the stabilization period required for the system to reach electrochemical equilibrium. Similar behavior of initial capacitance loss has also been observed in previous reports [34,35]. After preliminary cycles, the $CuHfSe_2$ electrode showed very promising stability features with no further loss in the capacitance, while the $HfSe_2$ electrode experienced ultimate 50% capacitance loss at the end of 5,000 cycles. It is well established that the stability of any diatomic transition metal sulfide/selenide is related to the ideal bond strength or the bond

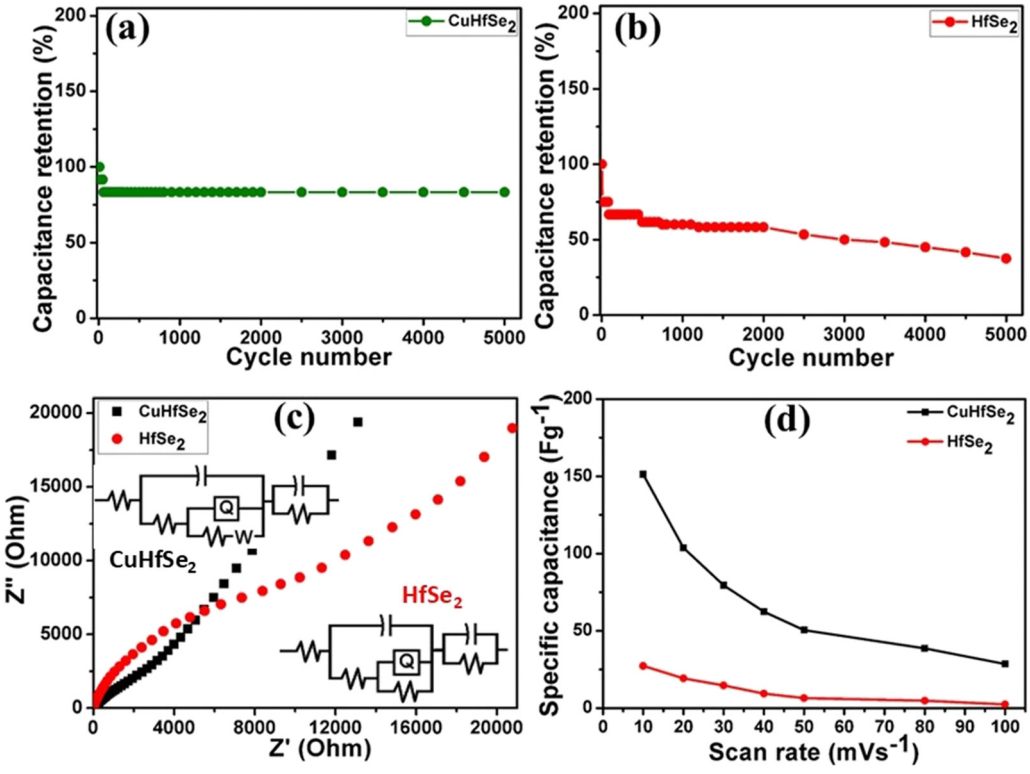

Figure 5: Capacitance retention for the (a) $CuHfSe_2$ and (b) $HfSe_2$ electrodes. (c) Electrochemical impedance spectroscopy and (d) specific capacitance *versus* scan rate curve.

Table 1: Comparison of the current work with previously published articles

Materials	Synthesis method	Additives	Electrolyte	No. of cycles	Capacitance retention (%)	Ref.
$HfSe_2$–$CuHfSe_2$	Chemical vapor transport	None	1 M H_2SO_4	5,000	85	Present work
MoS_2	Hydrothermal	Carbon black	3 M KOH	1,000	70	[45]
Ti_3C_2	Etching and mechanical mixing	Acetylene black	6 M KOH	6,000	88	[46]
MnO_2	Hydrothermal	Acetylene black	1 M Na_2SO_4	10,000	85	[47]
Graphene/GO/GrO nanocomposite	Ultrasonic-assisted liquid-phase exfoliation	Carbon black	1 M KOH	5,000	94	[24]
Mn-doped $SmCoO_3$	Hydrothermal	—	2 M KOH	5,000	—	[48]
Cu/MnX(O,S,C)-rGO	Direct oxidation, sulfidation, and carbonization	Acetylene black	3 M KOH	1,000	92	[25]
Activated carbon with carbon-based composites	Mechanical mixing	C60, Carbon black, activated carbon nanofiber, SWCNTs, graphene nanoplatelets	1 M Li_2SO_4	10,000	75, 82, 85, 95	[49]
ZrS_2 quantum dot	CBD	Carbon black	1 M KOH	—	—	[26]

dissociation energies of its constituent elements [36,37]. It has been reported that moduli (based on the force of stretching and strain between the bonds of the transition metals and chalcogen elements) of TMDCs increase on moving from lower-number groups to the higher-number groups [38]. A similar trend was observed in our synthesized TMDC materials, *i.e.*, compared to the undoped $HfSe_2$, after doping with Cu, the formation of its bond with the host selenium elements by replacing the Hf atoms, the overall bond strength of $CuHfSe_2$ is increased, which is eventually reflected in the stability test. Moreover, for the broader interest of readers, a comparison between the present work and some previously published articles is presented in Table 1.

After charging–discharging stability measurements, the morphological stability of the $CuHfSe_2$ electrode material was further confirmed by SEM, as shown in Figure S1. It is clear from the SEM image that there are no significant changes in the morphological structure of our grown material, which shows its stable behavior; however, due to the repeated charging and discharging cycles, a very small amount of nanosized lump formation can be seen on the material's surface. This formation may be due to the agglomeration of sulfate ions or minor sulfonation on the material surface. Moreover, XRD diffraction was performed to examine any structural changes in the tested electrode material, as shown in Figure S2. It was revealed that most of the peaks in the $CuHfSe_2$ spectra reappeared after electrochemical measurements with no significant changes, thus confirming the stability of the electrode material. The slight peak broadening is attributed to the ion agglomeration at the material surface, which is also evident from the SEM image. To further ascertain the characteristics of the electrode materials synthesized, electrochemical impedance spectroscopy (EIS) was conducted in the applied frequency range of 0.01–1 MHz, as shown in the Nyquist plot in Figure 5(c). It is well known that the higher curve in the lower frequency range of the EIS spectra (Warburg impedance) reflects better supercapacitive behavior [39–41]. In this regard, the $CuHfSe_2$ electrode illustrated better conductivity due to the addition of Cu, as compared to the undoped $HfSe_2$ electrode, which demonstrates a lower Warburg impedance. The effect of Cu doping was further investigated by analyzing the interface (R_s) and charge transfer resistance (R_{ct}) values using the measured EIS spectra. From the experimental EIS data and its simulation fitting, it was observed that the Cu-doped $HfSe_2$ electrode showed better conductivity with interfacial and charge transfer resistance values of 0.72 and 3.97 Ω, compared to the undoped $HfSe_2$ electrode, whose values were 0.87 and 5.6 Ω, respectively. EIS simulation and best

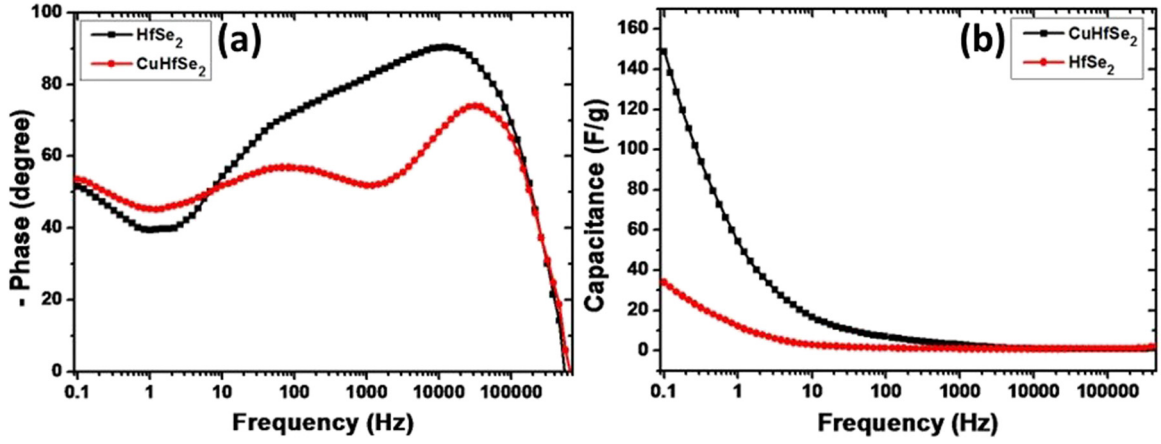

Figure 6: (a) Phase angle *versus* frequency and (b) capacitance *versus* frequency plots.

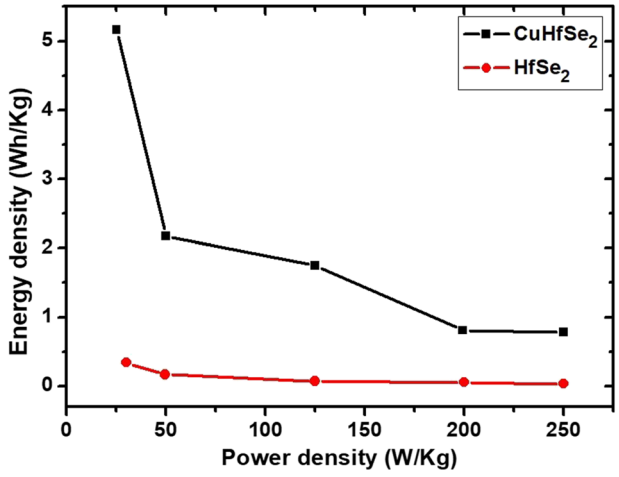

Figure 7: Power and energy densities comparison for the $HfSe_2$ and $CuHfSe_2$ electrodes.

curve fitting circuit models were also constructed, as shown in the EIS inset images. Figure 5(d) shows the capacitance *versus* scan rate trend, which was obtained from the measured cyclic voltammograms of the electrodes. The graphs of both electrode materials show a decrease in the capacitance trend with increasing scan rates. The observed trend is obvious because the increasing scan rate charges are swept at faster rates, which provides fewer chances for them to interact with the active electrode material, resulting in a decrease in the electrode capacitance [42].

The ideal supercapacitor device oscillates between a capacitor in the low-frequency region and a resistor in the high-frequency region [43]. Therefore, in order to examine the capacitive behavior of the prepared electrodes, Bode plots, showing phase angle–frequency trends, are shown in Figure 6(a). It can be observed that in the low-frequency region, the Cu-doped $HfSe_2$ electrode shows a higher phase angle compared to $HfSe_2$, with the calculated magnitudes of around 54° and 51°, respectively, at 0.1 Hz. To further understand the intrinsic behavior of our electrode materials, the range of frequencies *versus* capacitance is plotted in Figure 6(b). The capacitance was calculated by using the following equation [6]:

$$C = \frac{-1}{2\pi f z''}, \tag{2}$$

where f is the frequency and Z'' is the imaginary impedance. It is clear from the figure that the Cu-doped electrode showed a higher magnitude of capacitance for a wide range of frequencies, contrary to the undoped electrode. These observations are in accordance with the above-mentioned CV and charge–discharge results.

The Ragone plot showing energy and power densities comparison for $HfSe_2$ and $CuHfSe_2$ electrodes is shown in Figure 7. The energy and power density values were calculated from the charge–discharge curves at current densities of 0.1–1 A/g using the following equations [44]:

$$E = \frac{1}{2}CV^2 \tag{3}$$

and

$$P = \frac{E}{\Delta t} \tag{4}$$

where C and V are the specific capacitances measured from the charge/discharge curves and potential window, respectively, and Δt is the discharge time of one cycle. It was found that at a current density of 0.1 A/g, the $CuHfSe_2$ electrode had a highest energy density value of 5.16 W h/kg with a power density of 25 W/kg; on the other hand, the $HfSe_2$ electrode exhibits energy and power density values of 0.340 W h/kg and 30 W/kg, respectively. Both electrodes

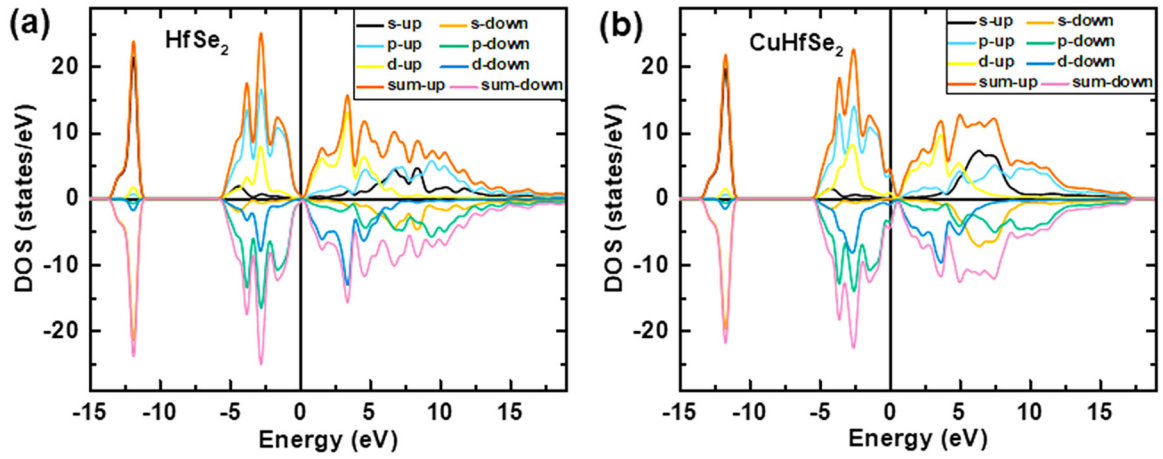

Figure 8: DFT-based PDOS calculations for the (a) $HfSe_2$ and (b) $CuHfSe_2$ materials.

exhibit a maximum power density value of 250 W/kg on reaching the current density value of 1 A/g, while the energy densities were 0.782 and 0.034 W h/kg for $CuHfSe_2$ and $HfSe_2$ electrodes, respectively.

Among semiconductor materials, those with higher conductivity can provide a greater number of charge carriers to participate in electrochemical reactions, making them more valuable as electrode materials for electrochemical supercapacitor applications. The enhanced performance of our $CuHfSe_2$ electrode material is related to its more conductive nature due to the addition of Cu metal, resulting in a reduction in impedance according to electrochemical impedance spectra. To further confirm this point, the role and contribution of Cu orbitals to the material's conduction and valence band electronic states were analyzed by calculating the band structure and PDOS, as shown in Figure 8. It can be seen in Figure 8(a) that $HfSe_2$ has a clear energy gap, which is a typical hallmark for semiconductor materials. The introduction of Cu atoms likely introduces additional states within the band gap, leading to a narrowing of the gap. As a result, the density of states of the valence band shifts and its upper edge significantly crosses the Fermi level. Figure 8(b) clearly reveals that after Cu doping, the band gap narrows and the valence band crosses the Fermi level. This implies that Cu-doped $HfSe_2$ behaves more like a semi-metal, where the Fermi level intersects the valence band, resulting in metallic conduction at the Fermi level, rather than semiconducting behavior, as typically observed in $HfSe_2$. The addition of Cu also increases the charge carrier density, and it also introduces additional energy levels within the band gap, effectively reducing the energy required for electrons to move from the valence band to the conduction band. These energy levels can hybridize with the existing ones, leading to a reduction in the band gap and a shift in the Fermi level. The hybridization of p-orbitals according to PDOS distributions in the valence bands is found to be a key contributor close to the Fermi level. Therefore, due to the crossing of the valence band and strong hybridization of p-orbitals near the Fermi level, it transformed toward a semimetal. The process of charge transfer became very swift in $CuHfSe_2$, which resulted in better electrochemical performance. Ultimately, the doping of Cu into $HfSe_2$ modifies its electronic structure. From these findings, it can be stated that the energy gap and charge carrier concentration close to the Fermi level play a vital role in determining the electronic conductivity of the grown material. Our density functional theory (DFT) calculation results agree with the experimental findings of electrochemical impedance spectroscopy and clearly verify that the enhanced energy storage response of the $CuHfSe_2$ material was due to its more conductive nature.

4 Conclusion

In this work, we report for the first time CVT-synthesized crystalline hafnium diselenide ($HfSe_2$) and its use for supercapacitor energy storage devices. Its potential was further explored by doping it with Cu metal ($CuHfSe_2$), which resulted in its efficiency enhancement by threefold after doping. A specific capacitance value of 44.7 F/g was estimated for the $HfSe_2$ electrode, and a significant increase of 151.83 F/g was observed at a scan rate of 10 mV/s after Cu doping. This enhanced capacitance value for the doped sample is due to increased layer spacing and conductivity due to Cu doping. Due to these factors, the $CuHfSe_2$ electrode surpassed the $HfSe_2$ electrode in terms of capacitance and stability features, as confirmed by the

experimental EIS analysis and DFT calculations. It is worth mentioning that the obtained capacitance values and other electrochemical analyses presented in the study reflect the pure intrinsic features of the materials, as no carbon additives were used for the electrode preparation, contrary to a common practice. The obtained values can be further enhanced manifold after adding carbon additives. Moreover, the grown $CuHfSe_2$ nanocrystals can be considered as a promising supercapacitor electrode material with good capacitance, stability, and energy density due to the unique microstructure of such 2D layered materials.

Acknowledgments: This work was funded by the Ongoing Research Funding program-Research Chairs (ORF-RC-2025-1502), King Saud University, Riyadh, Saudi Arabia.

Funding information: This work was funded by the Ongoing Research Funding program-Research Chairs (ORF-RC-2025-1502), King Saud University, Riyadh, Saudi Arabia.

Author contributions: All authors have accepted responsibility for the entire content of this manuscript and approved its submission.

Conflict of interest: The authors state no conflict of interest.

Data availability statement: The datasets generated and analyzed during the current study are available from the corresponding author on reasonable request.

References

[1] Winter M, Brodd RJ. What are batteries, fuel cells, and supercapacitors? Chem rev. 2004;104(10):4245–70.

[2] Wang S, Wei T, Qi Z. Supercapacitor energy storage technology and its application in renewable energy power generation system. Paper presented at: Proceedings of ISES World Congress 2007, vol. I–V, Solar Energy and Human Settlement, 2009.

[3] Yang P, Chao D, Zhu C, Xia X, Zhang Y, Wang X, et al. Ultrafast-charging supercapacitors based on corn-like titanium nitride nanostructures. Adv sci. 2016;3(6):1500299.

[4] Huang Y, Li Y, Hu Z, Wei G, Guo J, Liu J. A carbon modified MnO_2 nanosheet array as a stable high-capacitance supercapacitor electrode. J Mater Chem A. 2013;1(34):9809–13.

[5] He L, Liu Y, Li C, Yang D, Wang W, Yan W, et al. A low-cost Zn-based aqueous supercapacitor with high energy density. ACS Appl Energ Mater. 2019;2(8):5835–42.

[6] Habib M, Khalil A, Muhammad Z, Khan R, Wang C, Rehman Z, et al. WX2 (X = S, Se) single crystals: a highly stable material for supercapacitor applications. Electrochim Acta. 2017;258:71–9.

[7] Li N, Zhu X, Zhang C, Lai L, Jiang R, Zhu J. Controllable synthesis of different microstructured MnO_2 by a facile hydrothermal method for supercapacitors. J Alloy Compd. 2017;692:26–33.

[8] Khan R, Habib M, Gondal MA, Khalil A, Rehman ZU, Muhammad Z, et al. Facile synthesis of $CuFe_2O_4$–Fe_2O_3 composite for high-performance supercapacitor electrode applications. Mater Res Express. 2017;4(10):105501.

[9] Wang C, Liu D, Chen S, Sang Y, Haleem YA, Wu C, et al. All-carbon ultrafast supercapacitor by integrating multidimensional nanocarbons. Small. 2016;12(41):5684–91.

[10] Irfan S, Haleem YA, Usman M, Ahmad N, Arshad M, Irshad MI, et al. Validating superior electrochemical outcome for supercapacitor application through first-principles calculations. New J Chem. 2024;48(11):4982–94.

[11] Al-Enizi AM, Ubaidullah M, Ahmed J, Ahamad T, Ahmad T, Shaikh SF, et al. Synthesis of NiO_x@NPC composite for high-performance supercapacitor via waste PET plastic-derived Ni-MOF. Compos Part B: Eng. 2020;183:107655.

[12] Al-Enizi AM, Ahmed J, Ubaidullah M, Shaikh SF, Ahamad T, Naushad M, et al. Utilization of waste polyethylene terephthalate bottles to develop metal-organic frameworks for energy applications: A clean and feasible approach. J Clean Prod. 2020;248:119251.

[13] Ubaidullah M, Ahmed J, Ahamad T, Shaikh SF, Alshehri SM, Al-Enizi AM. Hydrothermal synthesis of novel nickel oxide@ nitrogenous mesoporous carbon nanocomposite using costless smoked cigarette filter for high performance supercapacitor. Mater Lett. 2020;266:127492.

[14] Habib M, Ullah S, Khan F, Rafiq MI, Salem Balobaid A, Alshahrani T, et al. Supercapacitor electrodes based on single crystal layered ZrX_2 (X = S, Se) using chemical vapor transport method. Mater Sci Eng: B. 2023;298:116904.

[15] Lin L, Lei W, Zhang S, Liu Y, Wallace GG, Chen J. Two-dimensional transition metal dichalcogenides in supercapacitors and secondary batteries. Energy Storage Mater. 2019;19:408–23.

[16] Habib M, Muhammad Z, Haleem YA, Farooq S, Nawaz R, Khalil A, et al. Bridging the gap: an in-depth comparison of CVT-grown layered transition metal dichalcogenides for supercapacitor applications. Mater Adv. 2024;5(3):1088–98.

[17] Khalil A, Liu Q, He Q, Xiang T, Liu D, Wang C, et al. Metallic 1T-WS_2 nanoribbons as highly conductive electrodes for supercapacitors. RSC Adv. 2016;6(54):48788–91.

[18] Zhang C, Ning J, Wang B, Guo H, Feng X, Shen X, et al. Hybridized 1T/2H-MoS_2/graphene fishnet tube for high-performance on-chip integrated micro-systems comprising supercapacitors and gas sensors. Nano Res. 2021;14:114–21.

[19] Saraf M, Natarajan K, Mobin SM. Emerging robust heterostructure of MoS_2–rGO for high-performance supercapacitors. ACS Appl Mater Inter. 2018;10(19):16588–95.

[20] Ahila M, Subramanian E. Influence of annealing on phase transformation and specific capacitance enhancement in Bi_2O_3. J Electroanal Chem. 2017;805:146–58.

[21] Mohan M, Shetti NP, Aminabhavi TM. Phase dependent performance of MoS_2 for supercapacitor applications. J Energy Storage. 2023;58:106321.

[22] Roberts AJ, Slade RC. Effect of specific surface area on capacitance in asymmetric carbon/α-MnO_2 supercapacitors. Electrochim Acta. 2010;55(25):7460–9.

[23] Sajedi-Moghaddam A, Mayorga-Martinez CC, Vaghasiya JV, Alduhaish O, Sofer Z, Pumera M. Structural manipulation of layered

TiS_2 to TiS_3 nanobelts through niobium doping for high-performance supercapacitors. Chem Electro Chem. 2020;7(24):4985–9.
[24] Zainab S, Fraz S, Awan SU, Hussain D, Rizwan S, Mehmood W. Optimized time dependent exfoliation of graphite for fabrication of Graphene/GO/GrO nanocomposite based pseudo-supercapacitor. Sci Rep-UK. 2023;13(1):14218.
[25] Tan S, Yao Z, Huang H, Liu Z, Guo S, Zhao X. High-performance supercapacitor electrode materials: Cu/MnXx (X = O, S, C)-rGO nanocomposites derived from CuMn-BTC metal–organic framework. J Electron Mater. 2025;53(3):1925–36.
[26] Gokulsaswath V, Suganya G, Monika S, Kalpana G. Investigation of zirconium disulphide quantum dots for supercapacitor applications. Cryst Res Technol. 2024;59(5):2300111.
[27] Skrodzki D, Molinaro M, Brown R, Moitra P, Pan D. Synthesis and bioapplication of emerging nanomaterials of Hafnium. ACS Nano. 2024;18(2):1289–324.
[28] Kang M, Rathi S, Lee I, Li L, Khan MA, Lim D, et al. Tunable electrical properties of multilayer $HfSe_2$ field effect transistors by oxygen plasma treatment. Nanoscale. 2017;9(4):1645–52.
[29] Habib M, Muhammad Z, Khan R, Wu C, Ur Rehman Z, Zhou Y, et al. Ferromagnetism in CVT grown tungsten diselenide single crystals with nickel doping. Nanotechnol. 2018;29(11):115701.
[30] Xiang Z, Zhang Z, Xu X, Zhang Q, Wang Q, Yuan C. Room-temperature ferromagnetism in Co doped MoS_2 sheets. Phys Chem Chem Phys. 2015;17(24):15822–8.
[31] Shannon RD. Revised effective ionic radii and systematic studies of interatomic distances in halides and chalcogenides. Acta Crystall A-Crys. 1976;32(5):751–67.
[32] Yue R, Barton AT, Zhu H, Azcatl A, Pena LF, Wang J, et al. $HfSe_2$ thin films: 2D transition metal dichalcogenides grown by molecular beam epitaxy. ACS Nano. 2015;9(1):474–80.
[33] Mirabelli G, McGeough C, Schmidt M, McCarthy EK, Monaghan S, Povey IM, et al. Air sensitivity of MoS_2, $MoSe_2$, $MoTe_2$, HfS_2, and $HfSe_2$. J Appl Phys. 2016;120(12):125102.
[34] Li H, Li H, Wu Z, Zhu L, Huang Y, Zhu X, et al. Phase engineering of $Mo_{1-x}WxS_2$ nanosheets for flexible supercapacitors. Scripta Mater. 2022;208:114346.
[35] Cao L, Yang S, Gao W, Liu Z, Gong Y, Ma L, et al. Direct laser-patterned micro-supercapacitors from paintable MoS_2 films. Small. 2013;9(17):2905–10.
[36] Griffith AA. The theory of rupture. Paper presented at: International Congress for Applied Mechanics, 1924.
[37] Li J, Medhekar NV, Shenoy VB. Bonding charge density and ultimate strength of monolayer transition metal dichalcogenides. J Phys Chem C. 2013;117(30):15842–8.
[38] Sun H, Agrawal P, Singh CV. A first-principles study of the relationship between modulus and ideal strength of single-layer, transition metal dichalcogenides. Mater Adv. 2021;2(20):6631–40.
[39] Taberna P, Simon P, Fauvarque J-F. Electrochemical characteristics and impedance spectroscopy studies of carbon-carbon supercapacitors. J Electrochem Soc. 2003;150(3):A292.
[40] Bhatt G, Singh G, Bhattacharya S. Basic principles of impedance spectroscopy. Impedance spectroscopy and its application in biological detection. Boca Raton, FL: CRC Press; 2023. p. 9–36.
[41] Shaheen F, Ahmad R, Sharif S, Habib M, Sharif R, Fatima M, et al. Polyaniline effect on rGO@ $NiPbTiO_3$ for enhanced supercapacitor performance. Mater Lett. 2021;284:129031.
[42] Ghosh K, Srivastava SK. Enhanced supercapacitor performance and electromagnetic interference shielding effectiveness of CuS quantum dots grown on reduced graphene oxide sheets. ACS Omega. 2021;6(7):4582–96.
[43] Kötz R, Carlen M. Principles and applications of electrochemical capacitors. Electrochim Acta. 2000;45(15–16):2483–98.
[44] Huang K-J, Wang L, Liu Y-J, Liu YM, Wang HB, Gan T, et al. Layered MoS_2–graphene composites for supercapacitor applications with enhanced capacitive performance. Int J Hydrogen Energy. 2013;38(32):14027–34.
[45] Gupta H, Chakrabarti S, Mothkuri S, Padya B, Rao T, Jain P. High performance supercapacitor based on 2D-MoS_2 nanostructures. Mater Today-Proc. 2020;26:20–4.
[46] Cao M, Wang F, Wang L, Wu W, Lv W, Zhu J. Room temperature oxidation of Ti_3C_2 MXene for supercapacitor electrodes. J Electrochem Soc. 2017;164(14):A3933–42.
[47] Wu X, Yang F, Dong H, Sui J, Zhang Q, Yu J, et al. Controllable synthesis of MnO_2 with different structures for supercapacitor electrodes. J Electroanal Chem. 2019;848:113332.
[48] Shehzad MF, Abdelbacki AM, Fatima J, Kumar A, Ali M, Kaur J. Development of Mn-doped $SmCoO_2$ electrode material for supercapacitor application. Mater Sci Eng: B. 2025;311:117795.
[49] Ayaganov Z, Pavlenko V, Haque SFB, Tanybayeva A, Ferraris J, Zakhidov A, et al. A comprehensive study on effect of carbon nanomaterials as conductive additives in EDLCs. J Energy Storage. 2024;78:110035.